Processing a Fe67Mo4.5Cr2.3Al2Si3C7P8.7B5.5 metallic glass: Experimental and computed TTT and CCT curves

(Article begins on next page)

07 January 2023

Processing a $Fe_{67}Mo_{4.5}Cr_{2.3}Al_2Si_3C_7P_{8.7}B_{5.5}$ metallic glass: experimental and computed TTT and CCT curves

Alberto Castellero[a],*, Gianluca Fiore[a], Nele Van Steenberge[b], Livio Battezzati[a]

[a] Dipartimento di Chimica & NIS, Università di Torino, 10125 Torino, Italy

[b] OCAS, NV, Pres. J.F. Kennedylaan 3, 9060 Zelzate, Belgium

*Corresponding Author. E-mail address: alberto.castellero@unito.it

Abstract

For metallic glass synthesis and processing the possible formation of crystals should be described by CCT curves. Motivated by results of the synthesis of wires of the $Fe_{67}Mo_{4.5}Cr_{2.3}Al_2Si_3C_7P_{8.7}B_{5.5}$ alloy by melt extraction, a methodology is proposed to compute TTT and CCT curves based on the classical nucleation and growth theory. The thermophysical parameters needed for the calculation are entirely derived from DSC experiments, including those expressing the Vogel-Fulcher-Tammann equation for viscosity. The critical cooling rate for amorphous wires is estimated and matched with the CCT curve. Then, the corresponding computed TTT curve is shown to reproduce well the experimental results of isothermal crystallization of the ribbons.

Keywords: Fe-based metallic glass; wire melt extraction; differential scanning calorimetry; thermophysical properties; TTT curve; CCT curve

1. Introduction

This paper reports on the experimental determination of the time-temperature-transformation (TTT) curve and calculation of both TTT and continuous cooling-transformation (CCT) curves for a Fe-based amorphous alloy, $Fe_{67}Mo_{4.5}Cr_{2.3}Al_2Si_3C_7P_{8.7}B_{5.5}$. Alloys in such multicomponent systems have good glass-forming tendency when synthesized using pure elements since bulk glasses have been reported of size up to cm [1], but glass production becomes more difficult when master alloys of commercial purity are employed [2, 3, 4]. Actually, on processing the alloy in melt extraction experiments aimed at making glassy wires from commercial purity materials, it was found that a fully glassy structure was formed only below a critical size. Since this process is inherently non-isothermal, a CCT curve should represent the behavior of the alloy in rapid cooling for

amorphization. The kinetics of devitrification has been treated for Fe-based glasses made by various technologies [1, 2, 3, 4, 5] but it has never been discussed for the melt extraction process [6].

It is worth mentioning that the processing of metallic glasses is evolving with the advent of additive manufacturing technologies [7] in which objects are built from feedstock material of small size: powders in selective laser melting [8, 9, 10], wire and foils [11, 12] in direct energy deposition. The local re-melting by means of the laser beam implies subsequently rapid solidification through heat conduction into the substrate. The possible formation of crystals should be described by CCT curves. However, significant multi-scale models have been elaborated for 3-D printing of Zr-based alloys employing finite element model to obtain temperature fields in powder bed fusion but combined with TTT calculation for devitrification [13, 14].

It has been demonstrated since long that the CCT curve can be obtained by analytical means from the TTT curve [15] which then remains the basis for studying the kinetics of phase formation. Following up previous analyses of the thermodynamic and transport properties of undercooled melts [16, 17], the present work proposes a method for computing TTT and CCT curves from meaningful evaluation of thermodynamic and kinetic properties of alloys and verifies the outcome with both isothermal and continuous heating experiments.

2. Experimental

The $Fe_{67}Mo_{4.5}Cr_{2.3}Al_2Si_3C_7P_{8.7}B_{5.5}$ alloy was prepared by vacuum induction melting at OCAS NV, using the raw materials listed in Table S1 in the Supporting Information. The resulting elemental main impurities are Cu and Mn in addition to the amount of inclusions expected in industrial steelmaking. The complex alloy composition was formulated to obtain a strong ferromagnetic glassy material.

An in-house made apparatus for melt extraction was employed to produce wires. The alloy is contained in a BN crucible which is slowly lifted towards a rapidly rotating Mo wheel machined on its circumference to make an angle of 60°. In the proximity of the wheel the alloy is induction melted to let the wheel extract a thin wire from it. Fig. 1 shows images of wires, one being approximately 50 μm in diameter and the other exceeding locally this size because of the occurrence of Rayleigh instability. The latter displays visible crystal patches on the surface. Also in cross section some crystal colonies are visible (Fig. S1 in Supporting Information). Ribbons were made by melt spinning having thickness of typically 30 μm. They resulted amorphous to microscopy and X-Ray Diffraction (XRD) inspection. DSC scans were performed with both type of samples. The fine wires and the ribbons gave very close traces (Fig. S2 in Supporting Information). Because of their shape the wires would not provide reliable results in XRD, therefore the ribbons were used

to identify the phases occurring in the samples at all processing stages working in Bragg-Brentano mode and employing Cu kα radiation.

DSC was employed with ribbon samples both isothermally to determine the TTT curve for crystallization, and in continuous heating mode at rates ranging from 0.5 to 80 K/min. Samples were always kept under flowing Ar from at least 15 minutes before scanning to complete cooling. The calibration of the DSC signal was repeatedly checked both for temperature and heat evolution/absorption during the experimental campaigns. High Temperature DSC (HTDSC) was employed to study the melting behavior of the alloy.

3. Results

The DSC results obtained at increasing heating rate are reported in Fig. 2. It is apparent that at rates up to 10 K/min a primary event occurs before the main peak due to a eutectic-like transformation. A single crystallization event takes place at higher rates. A transformation giving a low intensity signal is evidenced at high temperatures. A further exothermal broad signal occurs after the latter ending above 750 °C, i.e. beyond the temperature limit of conventional DSC equipment.

The zone of the transition from the glassy to supercooled liquid state of the alloy as a function of heating rate is reported in Fig. 3 which shows how the transition is shifted to progressively higher temperature. It is also seen that the jump in specific heat at T_g becomes higher on increasing heating rate. This is likely due to partial overlap of the endothermic T_g jump with the beginning of the exothermic primary crystallization at low heating rate, whereas on increasing heating rate, typically above 10 K/min, the crystallization peak shifts faster than the glass transition and the two phenomena do not overlap anymore. The specific heat difference, $\Delta C_{p,g}$, between the supercooled liquid and the glass at the glass transition levels off at the value of 0.31 ± 0.01 J/(gK).

The overall amount of heat evolved during the transformation events is reported in Fig. 4 as a function of the temperature of the maximum of the main peak. The enthalpy of crystallization increases on increasing temperature. The inset of Fig. 4 reports the melting behavior of the alloy together with the fraction liquid obtained by integrating the peaks. The 50% fraction is found at 1240 K which will be taken as a reference temperature for the liquid phase, T_m. The overall enthalpy of melting is 249 ± 6 J/g.

An example of DSC trace for isothermal crystallization at 768 K is shown in Fig. 5. After the instrumental transient, the first crystallization peak starts after annealing for about 600 s and is overlapped after about 7000 s by the second crystallization event ending approximately after 24000 s. The two peaks apparently correspond to those found on continuous heating at low rates. The third transformation could not be detected with precision isothermally. The isothermal DSC peaks begin at increasing time on decreasing

temperature. Therefore, the occurrence of an incubation time for crystallization is deduced within the instrumental resolution. The times for the start of transformations are collected for each temperature and reported in Fig. 6 which gives the experimental TTT curve for crystallization.

The crystalline phases produced by the two crystallization processes have been identified by analyzing samples after continuous heating up to selected temperatures, Fig. 7(a), and after isothermal annealing for selected times, Fig. 7(b). On heating a sample up to 849 K at 20 K/min the main crystal reflection seen in the XRD pattern is compatible with a primary austenite phase, (γ in Fig. 7) which forms together with a Fe_9P_2B-type phase during the following main eutectic crystallization event. After annealing beyond the last exothermal peak of Fig. 2, reflections compatible with a $M_{23}C_6$ compound are recognized. Since reflections are broad throughout, it cannot be ascertained whether a minority glassy phase remains after the second phase transformation and crystallizes at higher temperature or the formation of the last compound originates from a reaction/decomposition of the phases already existing. On isothermal annealing at 768 K the XRD pattern becomes slightly asymmetric after 7200 s and displays reflections of the γ phase overlapping the amorphous halo after 8400 s. After annealing samples up to 24000 s, the γ and Fe_9P_2B-type phases are identified and an amorphous halo seems to remain in the pattern.

The γ, Fe_9P_2B-type and $M_{23}C_6$ phases represent the equilibrium constitution of the alloy since no further transformation is detected before melting. Also the master alloy from which the ribbons were obtained contains the same phases which apparently form on solidification.

4. Discussion

The production of wires by melt extraction implies a liquid stream is extracted by the rotating wheel and ejected in the equipment chamber where the stream takes a circular cross section and is cooled below the glass transition by the gas contained in the chamber. This must occur before the stream subdivides in droplets because of Rayleigh instability or crystallizes. The cooling rate achieved in such processes has been modelled accounting for heat transfer to the surrounding medium for droplet atomization according to [18]

$$\frac{dT}{dt} = \frac{-6h\left(T - T_{gas}\right)}{\rho d C_p} \qquad (1)$$

where h is the heat transfer coefficient, T the alloy temperature, T_{gas} the temperature of the gas in the quenching chamber, ρ the alloy density, d the diameter of the wire instead of that of a droplet, and C_p the melt specific heat. With the parameters collected in Table 1 the cooling rate results $9.3 \cdot 10^4$ K/s.

The diameter of the wire chosen for calculation is that corresponding to the critical size for amorphization. When the size is larger because of the choice of process parameters and incipient balling due to Rayleigh

instability, crystals were found inside the material. Therefore, this critical cooling rate is expected to correspond to that computed from a continuous cooling transformation diagram.

4.1. Phases and phase evolution

The primary phase forming during crystallization of the alloy at low temperature is an austenitic solid solution. From the alloy composition in which all elements apart from C and P are ferrite formers, it is deduced that the austenite is C-rich since P has very limited solubility in γ-Fe. Actually, when the eutectic crystallization occurs the P is found together with B in the Fe_9P_2B compound. The austenite reflections in Fig. 7a decrease in intensity only after scanning a sample in DSC up to 983 K where a $M_{23}C_6$ carbide appears likely because of decomposition of the austenite. This is in agreement with previous findings both in rapidly solidified crystalline alloys [20, 21] and devitrified alloys [1]. Since at the highest heating rate employed in DSC scans, the crystallization occurs via a single peak, corresponding to a eutectic transformation, the crystallization from the melt is modeled in the following as a eutectic.

4.2. Alloy thermodynamics

The enthalpies for crystallization, ΔH_x, and melting, ΔH_m, are related by

$$\Delta H = \Delta H_m - \int_T^{T_m} \Delta C_p \, dT \tag{2}$$

where ΔC_p is the specific heat difference between the supercooled liquid and the equilibrium crystal phases. It is assumed here that ΔC_p is expressed by a hyperbolic function of temperature, $\Delta C_p = k/T$, in line with the assumption on viscosity explained below. Using the experimental $\Delta C_{p,g}$, the parameter k is 246 J/g. The DSC data provide a mean to estimate the average ΔC_p in the temperature range spanned by the peaks of Fig. 1, giving a value of 0.288 J/(gK) which measures the average specific heat difference between supercooled liquid and crystal phases. It is assumed here, as customary, that the specific heat of the glassy phase is close to that of the crystal phases. This is lower than $\Delta C_{p,g}$ showing that the present alloy conforms to the general behavior of metallic glass-formers in which the excess specific heat of the liquid increases on decreasing temperature [14]. From 837 K (the first peak temperature in Fig. 2) and 1240 K (the temperature at which 50% of liquid is formed) the average ΔC_p is accordingly lower, i. e. 0.238 J/(gK). The free energy difference between liquid and equilibrium crystal phases is computed according to

$$\Delta G = \Delta H_m - \int_T^{T_m} \Delta C_p \, dT - T\Delta S_m + T \int_T^{T_m} \Delta C_p \, \frac{dT}{T} \tag{3}$$

and converted to the free energy difference per unit volume, ΔG_v, needed to compute the activation barrier for nucleation, ΔG^*

$$\Delta G^* = \frac{16\pi}{3} f(\vartheta) \frac{\gamma^3}{\Delta G_v^2} \tag{4}$$

where γ is the solid-liquid interfacial free energy and $f(\theta)$ is a function of the wetting angle θ for heterogeneous nucleation [22]. The latter will be taken as an adjustable parameter in the following. The interfacial energy is computed by means of the following expression earlier derived for undercooled glass-forming systems [23]

$$\gamma = 0.24 + 0.29 * \frac{T}{T_m} \frac{\Delta H_m}{N_A^{1/3} V_m^{2/3}} \tag{5}$$

using the molar volume, V_m and the Avogadro constant, N_A.

4.3. Crystal nucleation

According to the classical theory [20], the nucleation frequency, I_v, is given on a molar basis by

$$I_v = \frac{24Dn^*}{a_0^2} Z N_A \exp(-\frac{\Delta G^*}{RT}) \tag{6}$$

where D is a diffusion coefficient, n^* is the number of atoms in the nucleus of critical size, a_0 a jump distance, R the gas constant, and Z the Zeldovich factor. n^* is computed from the size of the critical nucleus and Z is estimated to be of the order of 10^{-1} in the present case. The diffusion coefficient, D, is evaluated from the alloy viscosity, η, employing the Stokes-Einstein equation. For metallic glass-formers, the Vogel-Fulcher-Tammann (VFT) equation based on three parameters, η_0, B and T_o, is a suitable approximate function for the viscosity trend as a function of temperature

$$\eta = \eta_0 \exp(\frac{B}{T-T_0}) \tag{7}$$

The η_0 parameter giving the high temperature limit for viscosity is conventionally expressed as $\eta_0 = hN_A/V_m$ where h is the Planck constant. η_0 is $1.25 \cdot 10^{-6}$ Pa·s for the present alloy [24].

In case the difference in specific heat between undercooled liquid and glass is hyperbolic, the Adam-Gibbs equation for viscosity

$$\eta = A \exp(\frac{C}{T S_c}) \tag{8}$$

where A and C are constants and S_c is the liquid configurational entropy, reduces to the VFT equation establishing a link between thermodynamic and transport properties of the melt.

A method for obtaining the B and T_0 parameters was described in detail earlier [15] (Mcfarlane, 1982). In short, the fragility of the alloy, m, i. e. the derivative of the viscosity VFT function versus inverse temperature taken at T_g, is given by

$$m = \frac{BT_g}{2.3\left(T_g - T_0\right)^2}$$ (9)

The *m* parameter is derived from the temperature span from the onset to the end of the glass transition zone at the heating rate of 20 K/min, ΔT_g, [25]

$$m = \frac{2T_g}{\Delta T_g}$$ (10)

obtaining *m* = 52. The result is checked by means of the Angell empirical formula [26] using other experimental quantities

$$m = 56\frac{T_g \Delta C_{p,g}}{\Delta H_m}$$ (11)

Which gives *m* = 55. The temperature T_0 has been shown to depend on thermodynamic quantities in the limit of validity of the equivalence of the VFT with the Adam-Gibbs equation [27], becoming equal to the temperature of liquid vanishing entropy, T_K, therefore

$$m = 17\frac{T_g}{T_g - T_K}$$ (12)

T_0 results 536 K and the *B* parameter 10557 K.

4.4. TTT and CCT curves

The rate of growth of nuclei after reaching critical size is expressed by [20]

$$u_c = \frac{fD}{\lambda}\left[1 - exp\left(-\frac{\Delta G}{RT}\right)\right]$$ (13)

where f is the fraction of sites available for atomic attachment, and λ a diffusion distance of the order of interatomic spacings. The time for reaching a given transformed fraction at each temperature, *x(T)* is derived from

$$x(T) = 1 - \exp(-\frac{\pi}{3}I_v u_c^3 t^4)$$ (14)

Here, *x(T)*=10^{-6} is used for the TTT and CCT curves referring to the beginning of crystallization of the three-dimensional crystal seen in wires.

The same transformed fraction is obtained on continuous cooling at a rate *q* at temperatures satisfying the following equation [13]

$$x(T) = \left[\frac{1}{q}\int_{T_m}^{T}\frac{dT}{t_{100}(T)}\right]^4$$ (15)

where $t_{100}(T)$ is the time needed to complete the transformation at each temperature, T. When the cooling rate, q, becomes high enough that $x(T)$ is less than the established limit, the CCT curve is stopped.

The TTT and CCT curves for the beginning of crystallization of $Fe_{67}Mo_{4.5}Cr_{2.3}Al_2Si_3C_7P_{8.7}B_{5.5}$ computed with the set of parameters listed above are reported in Fig.8. In order to match the critical cooling rate for full amorphization of wires of $9.3 \cdot 10^4$ K/s corresponding to the end of the CCT curve, a wetting angle of 73° for heterogeneous nucleation must be assumed. With this assumption the TTT curve fits well the data on the beginning of crystallization in isothermal experiments in the temperature range accessible in DSC runs. As a sensitivity analysis of the present calculation, it is noted that should the nucleation be homogenous, the calculated TTT curve would fall far away from the experimental data, e. g. at 800 K the onset for isothermal crystallization should be around 84000 s, i.e. about 200 times the experimental value obtained in isothermal DSC measurement. The resulting value of the wetting angle, however, should be considered as indicative although not unrealistic. In fact, the computed TTT and CCT curves for a transformed fraction of 10^{-3} instead of 10^{-6} finding would match with experiments for a wetting angle of 66° instead of 73°.

5. Conclusions

Wires and ribbons of the $Fe_{67}Mo_{4.5}Cr_{2.3}Al_2Si_3C_7P_{8.7}B_{5.5}$ alloys were synthesized employing raw materials of commercial purity. A critical size for amorphization of 50 μm was found for wires made by melt extraction in Argon atmosphere. Since both wires and ribbons showed the same crystallization behavior, they were considered equivalent in this work.

The thermodynamic and kinetic parameters for the calculation of the nucleation frequency and growth rate have been fully determined from a set of DSC measurements of the glass transition, crystallization and melting temperatures, and of the enthalpy of crystallization and melting. Using proper correlations among parameters, the correspondence between the thermodynamic and kinetic fragility of the melt was ascertained, therefore the atomic mobility of the liquid could be estimated without resorting to viscosity measurement.

Finally, CCT and TTT curves for amorphization and crystallization have been computed. At first, the CCT curve has been matched with the results of the critical diameter of wires produced in melt extraction, by adjusting the wetting angle as an arbitrary parameter. Subsequently, the TTT curve has been compared with the time for the beginning of isothermal crystallization in DSC experiments made with thin melt spun ribbons finding good correspondence and, therefore, validating the computing procedure.

References

[1] B. Botchtler, O. Gros, I. Gallino, R. Busch, Thermo-physical characterization of the $Fe_{67}Mo_6Cr_{3.5}Ni_{3.5}P_{128}C_{5.5}B_{2.5}$ bulk metallic glass forming alloy, Acta Mater. 118 (2016) 129-139. https://doi.org/10.1016/j.actamat.2016.07.031.

[2] H.X. Li, Z.P. Lu, S.H. Yi, Estimation of the Glass Forming Ability of the Fe-based Bulk Metallic Glass $Fe_{68.8}C_{7.0}Si_{3.5}B_{5.0}P_{9.6}Cr_{2.1}Mo_{2.0}Al_{2.0}$ that Contains Non-metallic Inclusions, Met. Mater. Int. 15 (2009) 7-14. https://doi.org/10.1007/s12540-009-0007-x.

[3] G.C. Lavorato, G. Fiore, A. Castellero, M. Baricco, J.A. Moya, Preparation and characterization of Fe-based bulk metallic glasses in plate form, Physica B 407 (2012) 3192–3195. https://doi.org/10.1016/j.physb.2011.12.062

[4] L.H. Liu, J. Ma, C.Y. Yu, X.S. Huang, L.J. He, L.C. Zhang, P.J. Li, Z.Y. Liu, Determination of forming ability of high pressure die casting for Zr-based metallic glass, J. Mater. Process. Technol. 244 (2017) 87–96. https://doi.org/10.1016/j.jmatprotec.2017.01.015.

[5] G. Fiore, M. Baricco, L. Martino, M. Coisson, P. Tiberto, F. Vinai, L. Battezzati, Formation, Time–Temperature–Transformation curves and magnetic properties of FeCoNbSiBP metallic glasses, J. Alloys Compd. 619 (2015) 437-442. https://doi.org/10.1016/j.jallcom.2014.08.260.

[6] J. Yi, 2018. Fabrication and Properties of Micro- and Nanoscale Metallic Glassy Wires: A Review. Adv. Eng. Mater. 20, 1700875. https://doi.org/10.1002/adem.201700875.

[7] S. Pauly, L. Loeber, R. Petters, M. Stoica, S. Scudino, U. Kuehn, J. Eckert, Processing metallic glasses by selective laser melting, Mater. Today 16 (2013) 38-41. https://doi.org/10.1016/j.mattod.2013.01.018,

[8] D. Ouyang, W. Xing, N. Li, Y. Li, L. Liu, Structural evolutions in 3D-printed Fe-based metallic glass fabricated by selective laser melting, Addit. Manuf. 23 (2018) 246–252. https://doi.org/10.1016/j.addma.2018.08.020.

[9] D.C. Hofmann, P. Bordeenithikasem, A. Pate, S.N. Roberts, E. Vogli, 2018. Developing Processing Parameters and Characterizing Microstructure and Properties of an Additively Manufactured FeCrMoBC Metallic Glass Forming Alloy. Adv. Eng. Mater. 20, 1800433. https://doi.org/10.1002/adem.201800433.

[10] Ł. Zrodowski, B. Wysocki, R. Wroblewski, A. Krawczynska, B. Adamczyk-Cieslak, J. Zdunek, P. Błyskun, J. Ferenc, M. Leonowicz, W. Swieszkowski, New approach to amorphization of alloys with low glass forming ability via selective laser melting, J. Alloys Compd. 771 (2019) 769-776. https://doi.org/10.1016/j.jallcom.2018.08.075.

[11] Y. Li, Y. Shen, C. Chen, M.C. Leu, H.-L. Tsai, Building metallic glass structures on crystalline metal substrates by laserfoil-printing additive manufacturing, J. Mater. Process. Technol. 248 (2017) 249–261. https://doi.org/10.1016/j.jmatprotec.2017.05.032.

[12] P. Bordeenithikasem, Y. Shen, H.-L. Tsai, D.C. Hofmann, Enhanced mechanical properties of additively manufactured bulk metallic glasses produced through laser foil printing from continuous sheetmetal feedstock, Addit. Manuf. 19 (2018) 95–103. https://doi.org/10.1016/j.addma.2017.11.010.

[13] Y. Lu, H. Zhang, H. Li, H. Xu, G. Huang, Z. Qin, X. Lu, Crystallization prediction on laser three-dimensional printing of Zr-based bulk metallic glass, J. Non-cryst. Solids 461 (2017) 12–17. https://doi.org/10.1016/j.jnoncrysol.2017.01.038.

[14] J. Lindwall, V. Pacheco, M. Sahlberg, A. Lundbäck, L.-E. Lindgren, Thermal simulation and phase modeling of bulk metallic glass in the powder bed fusion process, Addit. Manuf. 27 (2019) 345–352. https://doi.org/10.1007/s11837-018-2919-8.

[15] D.R. Mcfarlane, Continuous cooling (CT) diagrams and critical cooling rates: A direct method of calculation using the concept of additivity, J. Non-Cryst. Solids 53 (1982) 61-72. https://doi.org/10.1016/0022-3093(82)90018-7.

[16] M. Palumbo, L. Battezzati, Thermodynamics and kinetics of metallic amorphous phases in the framework of the CALPHAD approach, CALPHAD 32 (2008) 295-314. https://doi.org/10.1016/j.calphad.2007.12.002.

[17] G. Dalla Fontana, A. Castellero, L. Battezzati, Thermodynamics and fragility of Fe-based glass forming melts, J. Non-Cryst. Solids 433 (2016) 103–108. https://doi.org/10.1016/j.jnoncrysol.2015.06.006.

[18] J.B. Wiskel, H. Henein, E. Maire, Solidification study of aluminum alloys using impulse atomization: Part I: Heat transfer analysis of an atomized droplet, Can. Metall. Q. 41 (2002) 97-110. https://doi.org/10.1179/cmq.2002.41.1.97

[19] R. Mehrabian, Relationship of heat flow to structure in rapid solidification processing, in: R. Mehrabian, B.H. Kear, M. Cohen (Eds.), Rapid Solidification Processing – I, Claitor's Pub., Baton Rouge, Louisiana, 1977, pp. 9-27.

[20] T. Minemura, A. Inoue, Y. Kojima, T. Masumoto, Formation of metastable austenite in splat quenched high alloy steels containing Cr, Mo, or W, Metall. Trans. A 11 (1980) 671-673. https://doi.org/10.1007/BF02670705.

[21] P.A. Molian, W.E. Wood, Formation of austenite in laser-processed Fe-0.2%C-20%Cr alloy, Mater. Sci. Eng. 56 (1982) 271-277. https://doi.org/10.1016/0025-5416(82)90103-3.

[22] I. Gutzow, J. Schmelzer, The Vitreous State: Thermodynamics, Rheology, and Crystallization. Springer, Berlin, 1995.

[23] L. Battezzati, Thermodynamic quantities in nucleation, Mater. Sci. Eng. A 304-306 (2001) 103-107. https://doi.org/10.1016/S0921-5093(00)01459-3.

[24] R. Busch, E. Bakke, W.L. Johnson, Viscosity of the supercooled liquid and relaxation at the glass transition of the $Zr_{46.75}Ti_{8.25}Cu_{7.5}Ni_{10}Be_{27.5}$ bulk metallic glass forming alloy, Acta Mater. 46 (1998) 4725-4732. https://doi.org/10.1016/S1359-6454(98)00122-0.

[25] C.T. Moynihan, Correlation between the Width of the Glass Transition Region and the Temperature Dependence of the Viscosity of High-Tg Glasses, J. Am. Ceram. Soc. 76 (1993) 1081-1087. https://doi.org/10.1111/j.1151-2916.1993.tb03724.x.

[26] L.-M. Wang, C.A. Angell, R. Richert, 2006. Fragility and thermodynamics in nonpolymeric glass-forming liquids. J. Chem. Phys. 125, 074505. https://doi.org/10.1063/1.2244551.

[27] L. Battezzati, G. Dalla Fontana, Thermodynamics and fragility of glass-forming alloys, J. Alloys Compd. 586 (2014) S9–S13. https://doi.org/10.1016/j.jallcom.2012.10.027.

Table Captions

Table 1. Properties used for computing cooling rate of the liquid in the melt extraction process by means of Eq. (1).

Table 1

Property	Value	References and notes
Heat transfer coefficient, h	9600 J/(m^{2}sK)	Value for Ar atomizing [19]
Gas temperature, T_{gas}	298 K	
Alloy density, ρ	7250 Kg/m^3	Experimental value of similar alloy [2]
Average atomic weight of alloy	47,6 g/mol	
Liquid specific heat, C_p	40.0 J/(molK)	This work
Critical wire diameter	50 μm	This work

Figures Captions

Fig. 1. SEM image of portions of melt extracted wires. The wire in the bottom part of the figure displays variation in thickness due to Rayleigh instability and signs of crystallization on the external surface where spots are apparent contrary to thinner wire on the top. The spots have been checked by EDS to ascertain they are not impurity particles.

Fig. 2. Normalized DSC traces showing the thermal effect of phase transformations in the $Fe_{67}Mo_{4.5}Cr_{2.3}Al_2Si_3C_7P_{8.7}B_{5.5}$ alloy. The traces shifted progressively at higher temperature since they were obtained at the increasing heating rates of 0.5 K/min (black), 3 K/min (green), 5 K/min (red), 10 K/min (magenta), 20 K/min (blue), 40 K/min (navy), 80 K/min (orange), respectively.

Fig. 3. Enlarged view of the normalized DSC traces of Fig. 2 showing the glass transition range. Colours as in Fig. 2.

Fig. 4. The total enthalpy of crystallization of the $Fe_{67}Mo_{4.5}Cr_{2.3}Al_2Si_3C_7P_{8.7}B_{5.5}$ alloy obtained by integrating the peaks reported in Fig. 2 and those found in high temperature scans above the limit of conventional DSC (see text). The continuous curve gives the result of the calculation of enthalpy of crystallization according to eq. 1 with error bars referring to the experimental uncertainty in the specific heat difference between liquid and crystal phases and in the heat of fusion. The inset shows the melting behaviour of the alloy. The transformed fraction was obtained by integrating the peaks.

Fig. 5. Example of isothermal DSC output for crystallization of the $Fe_{67}Mo_{4.5}Cr_{2.3}Al_2Si_3C_7P_{8.7}B_{5.5}$ alloy. The trace was obtained when annealing at 768 K.

Fig. 6. Experimental time-temperature-transformation results for the beginning of crystallization of the $Fe_{67}Mo_{4.5}Cr_{2.3}Al_2Si_3C_7P_{8.7}B_{5.5}$ alloy at various temperatures.

Fig. 7. (a) XRD patterns taken with samples of the $Fe_{67}Mo_{4.5}Cr_{2.3}Al_2Si_3C_7P_{8.7}B_{5.5}$ alloy heated in DSC up to selected temperatures at the heating rate of 20 K/min. Legend: a. 849 K; b. 859 K; c. 893 K; d. 983 K; e. as spun. (b) XRD patterns taken with samples of the $Fe_{67}Mo_{4.5}Cr_{2.3}Al_2Si_3C_7P_{8.7}B_{5.5}$ alloy annealed in DSC at 768 K for the following times: a. 4800 s; b. 6000 s; c. 7200 s; d. 8400 s; e. 10800 s; f. 12600 s; g. 15600 s; h. 24000 s.

Fig. 8. Computed TTT (red) and CCT (blue) curves for the beginning of crystallization of the $Fe_{67}Mo_{4.5}Cr_{2.3}Al_2Si_3C_7P_{8.7}B_{5.5}$ alloy. The experimental data of Fig.6 are reported as well.

Figure 1
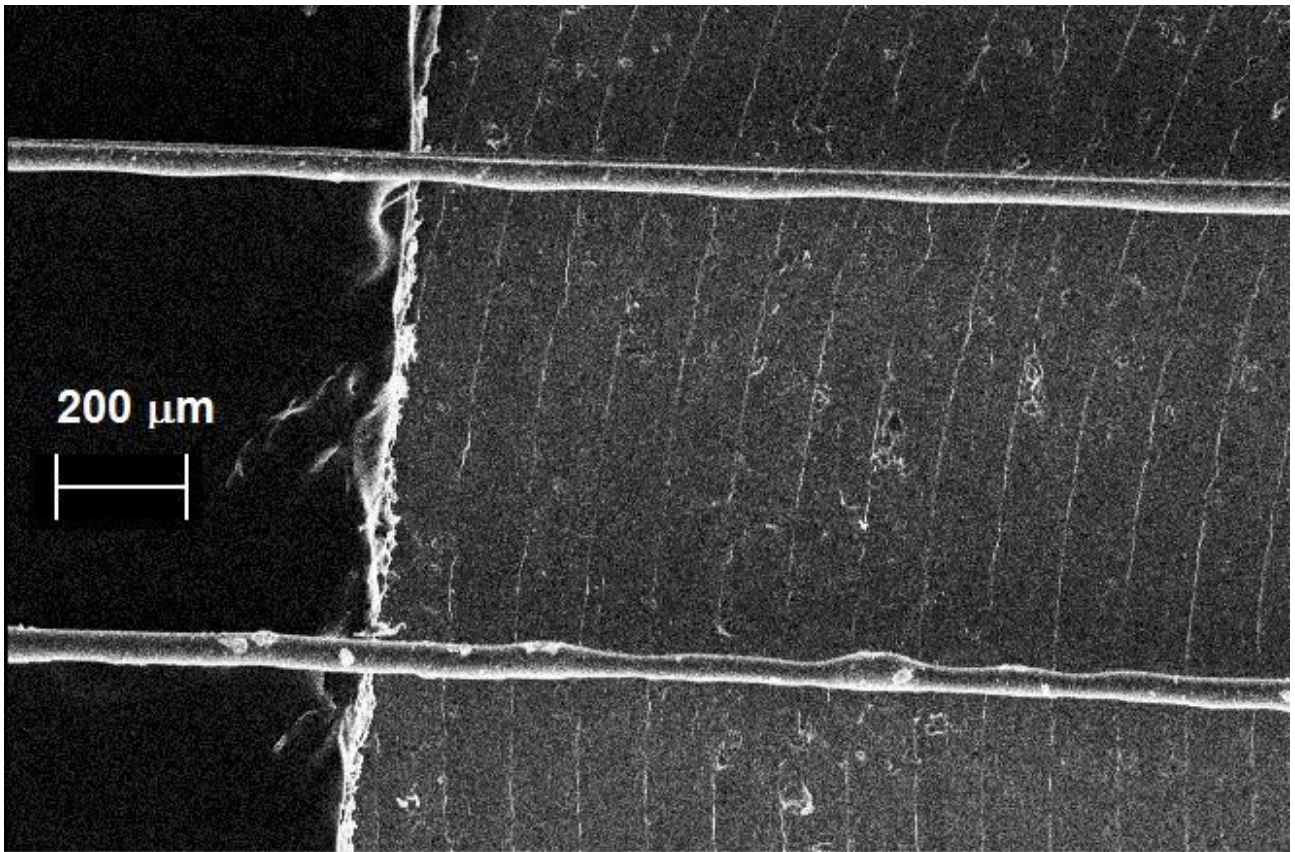
Figure 2
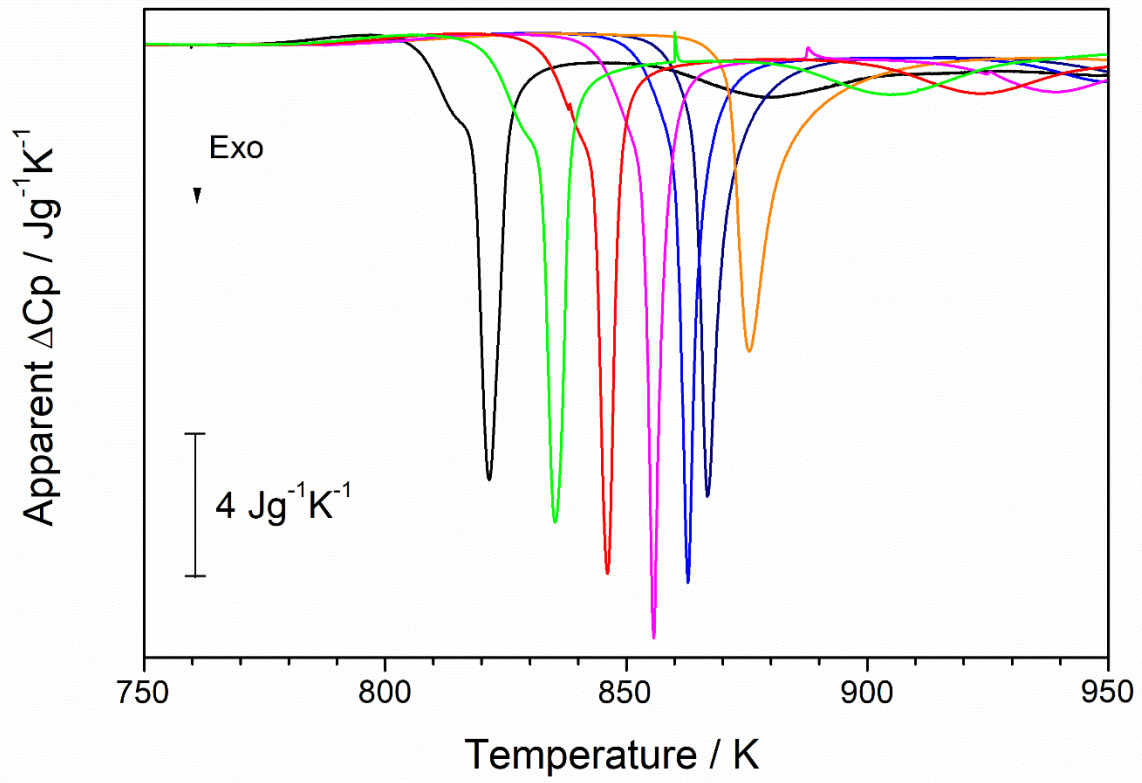
Figure 3
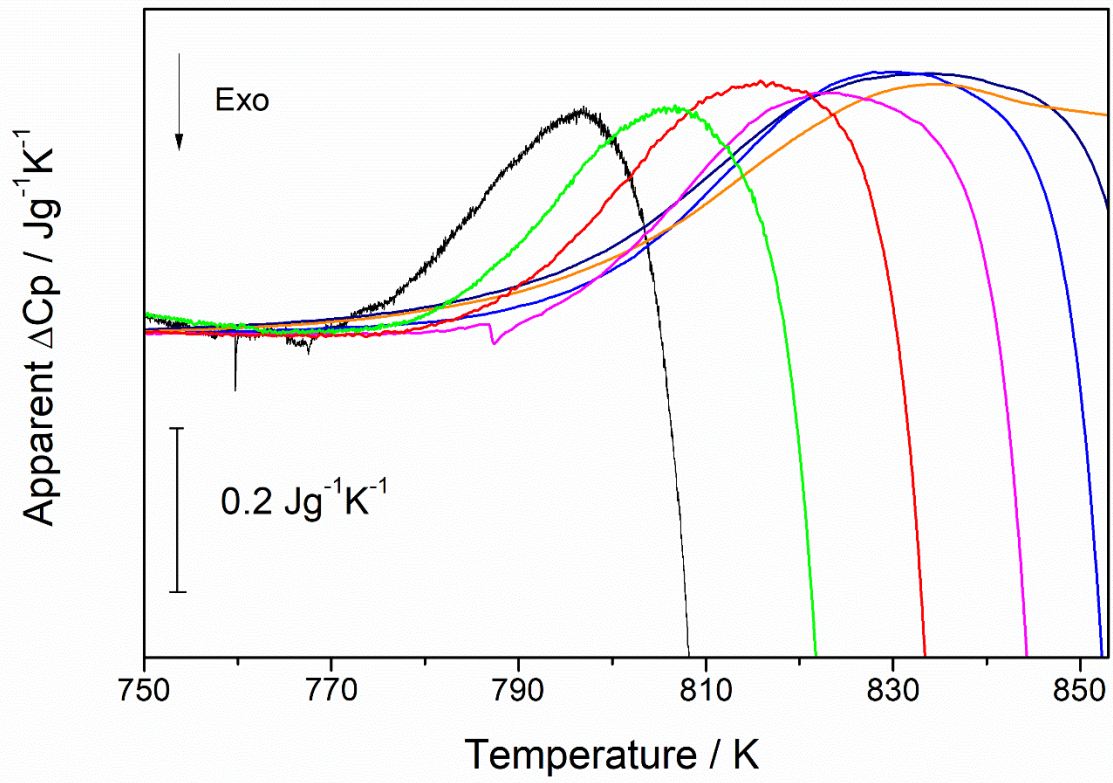
Figure 4
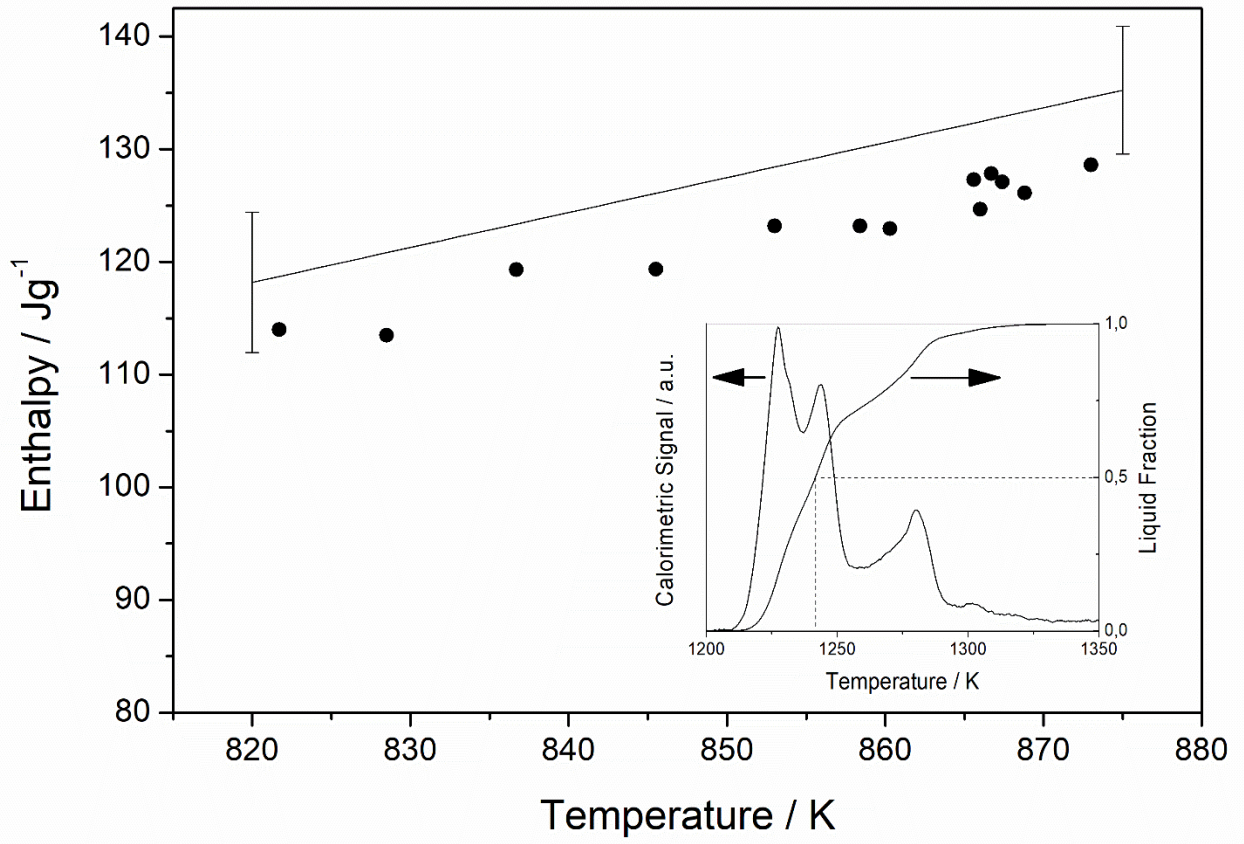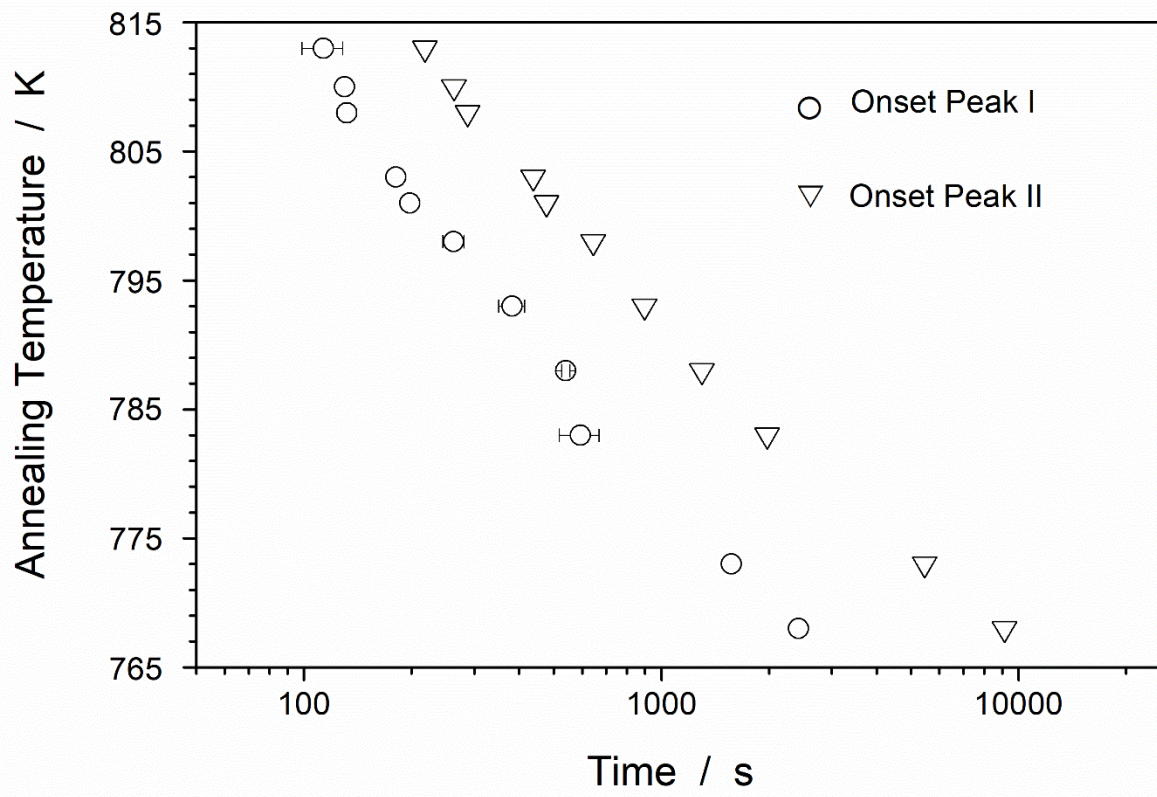
Figure 5
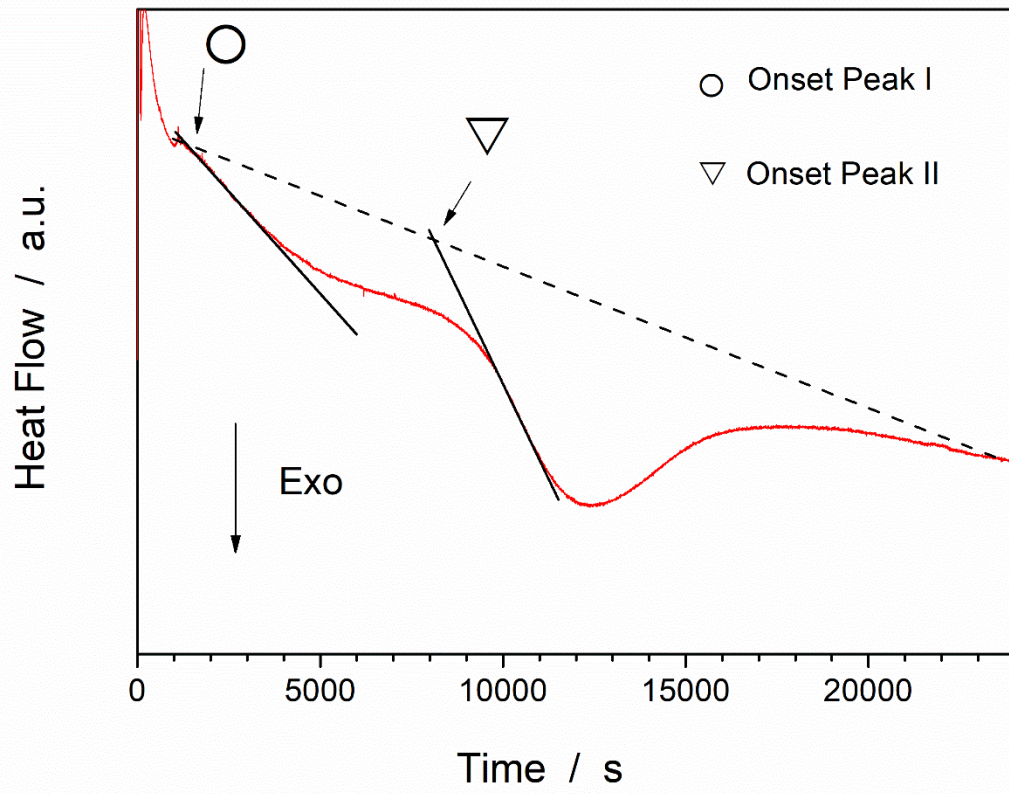
Figure 6

Figure 7
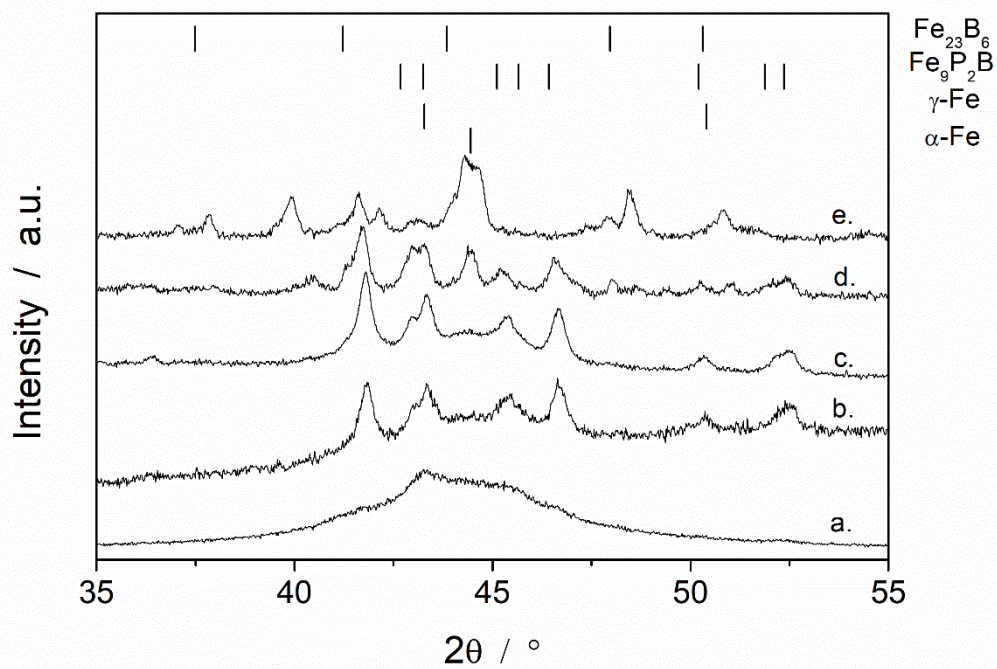
(a)
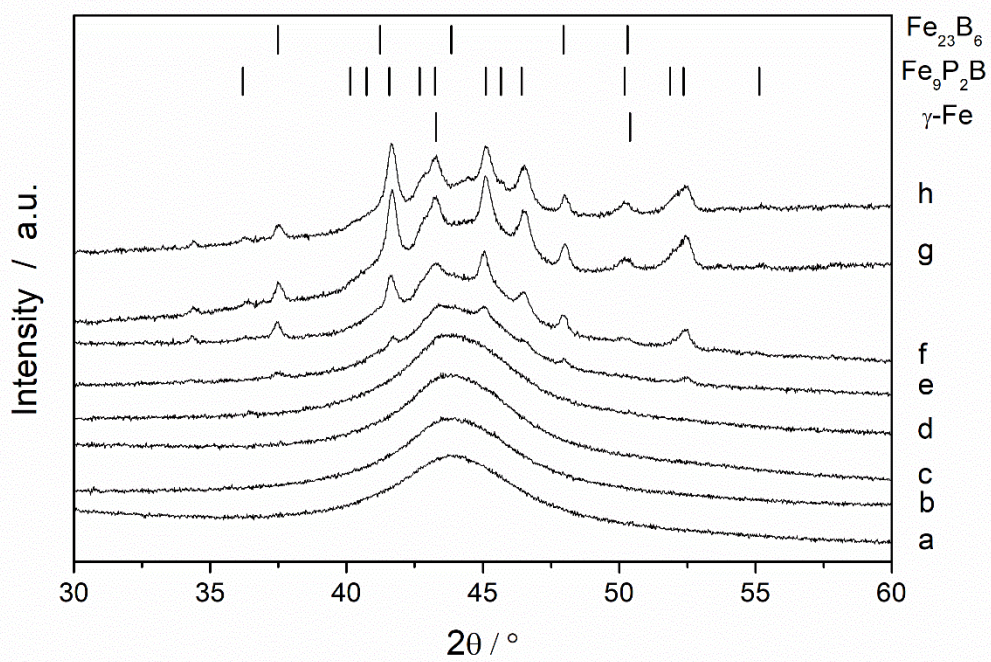
(b)

Figure 8
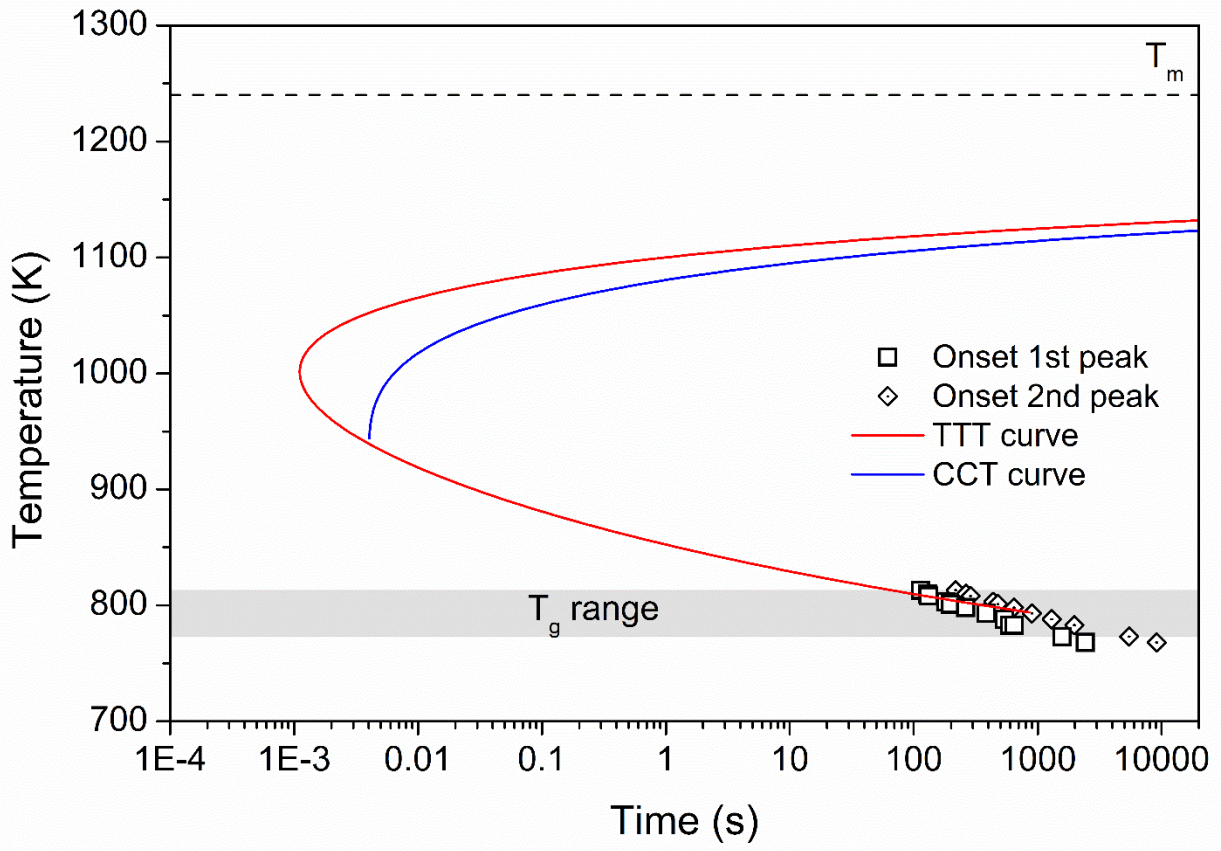
Supplementary material

Processing a Fe$_{67}$Mo$_{4.5}$Cr$_{2.3}$Al$_2$Si$_3$C$_7$P$_{8.7}$B$_{5.5}$ metallic glass: experimental and computed TTT and CCT curves

Alberto Castellero[a],*, Gianluca Fiore[a], Nele Van Steenberge[b], Livio Battezzati[a]

[a] Dipartimento di Chimica & NIS, Università di Torino, Torino, Italy

[b] OCAS, NV, Pres. J.F. Kennedylaan 3, 9060 Zelzate, Belgium

*Corresponding Author. E-mail address: alberto.castellero@unito.it

Table S1. Raw materials used for the synthesis of the $Fe_{67}Mo_{4.5}Cr_{2.3}Al_2Si_3C_7P_{8.7}B_{5.5}$ alloy.

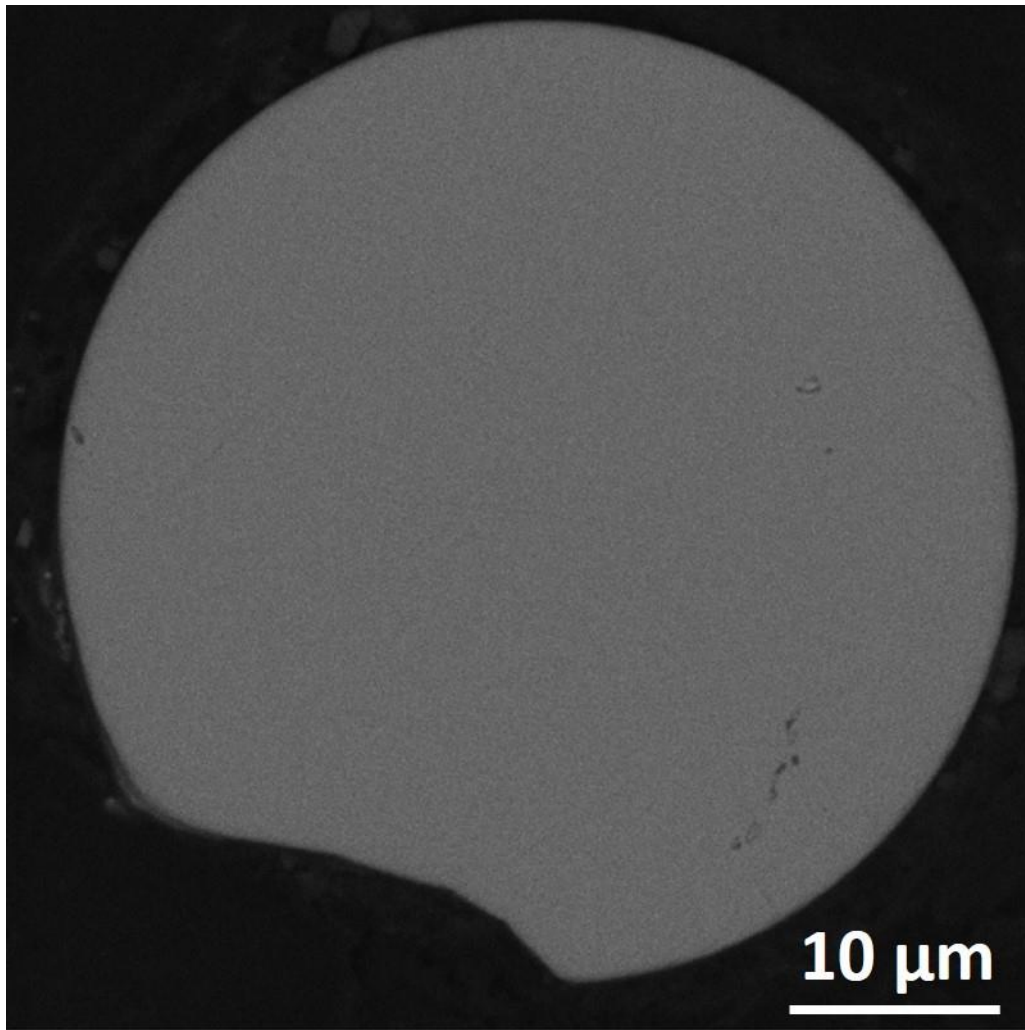| Element	Raw material	Purity, wt %	Main impurities in raw material
Fe	Fe	99,99	Oxygen
P	FeP, with ~ 25.7% P	95% (sum of Fe+P)	Mn, Si, Cr
Cr	commercial purity Cr	99.82%	Fe
Mo	FeMo with ~ 69.16% Mo	99.0% (sum of Fe+Mo)	Cu, Si
Al	commercial purity Al	98%	Fe, Si, Mn, Cu
Si	FeSi with 75% Si	99.9% (sum of Fe+Si)	
C	graphite		
B	FeB with 20% B	98% (sum of Fe+B)	C, Si, Al

Fig. S1. Back Scattered Electron image of the cross section of a melt extracted wire 45 μm in diameter. The dark spots are due to shrinkage consequent to crystal formation.
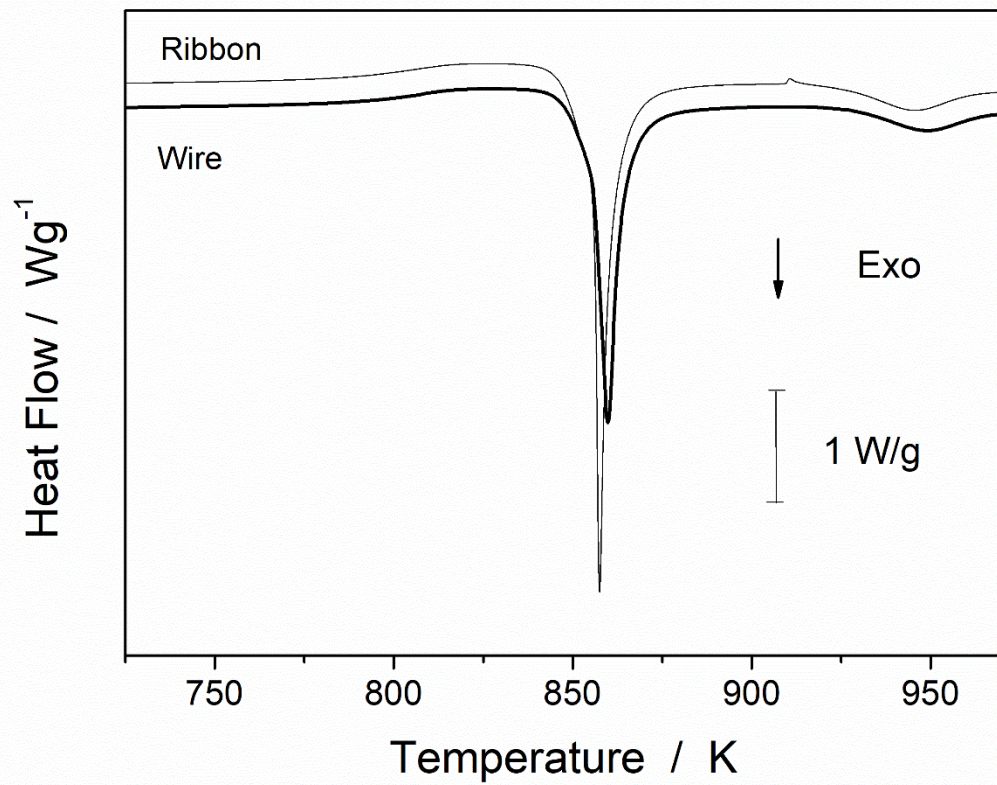
Fig. S2. DSC traces given by ribbon and wire samples of the $Fe_{67}Mo_{4.5}Cr_{2.3}Al_2Si_3C_7P_{8.7}B_{5.5}$ alloy (heating rate of 20 K/min). The peak given by the wire is shifted to lower temperature of a few degrees with respect to those given by the ribbon as expected in the presence of a crystallized fraction.